GLIA

WILEY

RESEARCH ARTICLE

Heterogeneity of astrocytes: Electrophysiological properties of juxtavascular astrocytes before and after brain injury

Stefanie Götz[1,2,3] | Ana Bribian[4] | Laura López-Mascaraque[4] |
Magdalena Götz[3,5,6] | Benedikt Grothe[1,3] | Lars Kunz[1]

[1]Division of Neurobiology, Department of Biology II, Ludwig-Maximilians-Universitaet (LMU) Munich, Martinsried, Germany

[2]Graduate School of Systemic Neurosciences, Ludwig-Maximilians-Universitaet (LMU) Munich, Martinsried, Germany

[3]Biomedical Center (BMC), Ludwig-Maximilians-Universitaet (LMU) Munich, SyNergy – Munich Cluster for Systems Neurology, Munich, Germany

[4]Instituto Cajal-CSIC, Molecular, Cellular and Developmental Neurobiology Department, Madrid, Spain

[5]Physiological Genomics, Biomedical Center (BMC), Ludwig-Maximilians-Universitaet (LMU) Munich, Martinsried, Germany

[6]Institute of Stem Cell Research, Helmholtz Center Munich, German Research Center for Environmental Health, Martinsried, Germany

Correspondence

Magdalena Götz, Physiological Genomics, Biomedical center (BMC), Ludwig-Maximilians-Universitaet (LMU) Munich, Martinsried, Germany.
Email: magdalena.goetz@helmholtz-muenchen.de

Benedikt Grothe, Division of Neurobiology, Department of Biology II, Ludwig-Maximilians-Universitaet (LMU) Munich, Martinsried, Germany.
Email: grothe@lmu.de

Lars Kunz, Division of Neurobiology, Department of Biology II, Ludwig-Maximilians-Universitaet (LMU) Munich, Martinsried, Germany.
Email: Lars.Kunz@bio.lmu.de

Abstract

Astrocyte heterogeneity is increasingly recognized, but still little is known about juxtavascular astrocytes with their somata directly adjacent to blood vessels, despite their importance after brain injury. As juxtavascular astrocytes originate from common progenitor cells, that is, have a clonal origin, they may intrinsically differ from other, non-juxtavascular astrocytes. To explore this, we examined the electrophysiological properties of these groups of astrocytes and the underlying ion channels. Using brain slices of BAC Aldh1l1-eGFP transgenic mice with astrocytes labeled by GFP expression, we compared juxtavascular and non-juxtavascular astrocytes in the somatosensory cortex by means of whole-cell patch-clamp recordings and immunohistochemical staining. Prior to injury, juxta- and non-juxtavascular astrocytes exhibit comparable electrophysiological properties with characteristic mostly passive conductance and a typical negative resting membrane potential. Immunohistochemical analysis of K$^+$ channels showed that all astrocytes were K$_{ir}$4.1$^+$, but revealed an intriguing difference for K$_v$4.3. The expression of K$_v$4.3 in sibling astrocytes (non-juxtavascular, juxtavascular and pial) was dependent on their ontogenetic origin with lowest levels in juxtavascular astrocytes located in upper cortical layers. After traumatic brain injury (TBI), we found profound changes in the electrophysiological type of astrocytes with a predominance of non-passive properties and this pattern was significantly enriched in juxtavascular astrocytes. This was accompanied by pronounced down-regulation of K$_{ir}$4.1 in proliferating astrocytes, which was significantly more in juxtavascular compared to non-juxtavascular astrocytes. Taken together, TBI induces profound differences in electrophysiological properties between juxtavascular and non-juxtavascular astrocytes that might be related to the preponderance of juxtavascular astrocyte proliferation.

1 | INTRODUCTION

Astrocytes play key roles in the healthy and diseased brain. Some of these are closely related to their unique passive membrane properties with high K^+ conductance, such as their role in K^+ buffering and glutamate up-take (Seifert, Henneberger, & Steinhauser, 2018; Verkhratsky & Nedergaard, 2018). K_{ir} channels are main players in mediating the typical resting potential of astrocytes close to the K^+ equilibrium potential (Verkhratsky & Nedergaard, 2018). $K_{ir}4.1$ channels are up-regulated when astrocyte progenitors stop to proliferate and mature during post-natal stages (Bordey & Sontheimer, 1997; Sontheimer, 1994). Moreover, $K_{ir}4.1$ levels define functional subpopulations of astrocytes in the spinal cord, highlighting their importance in astrocyte function (Kelley et al., 2018). Conversely, $K_{ir}4.1$ has been found to be down-regulated in several injury conditions (Kelley et al., 2018; Nwaobi, Cuddapah, Patterson, Randolph, & Olsen, 2016), when astrocytes become reactive and some astrocytes initiate proliferation (Frik et al., 2018; Robel, Berninger, & Gotz, 2011; Sirko et al., 2013). Notably, after traumatic brain injury (TBI) in the cerebral cortex proliferating reactive astrocytes are predominantly located with their somata at the blood vessels (Bardehle et al., 2013; Sirko et al., 2013), which serves two important functions, namely to exclude invading monocytes and to re-establish the blood brain barrier (Bush et al., 1999; Frik et al., 2018). We refer to these astrocytes as juxtavascular (rather than perivascular) as their somata are tightly associated to the blood vessels, but are not located in the perivascular space (Bardehle et al., 2013).

This prompts the question if juxtavascular astrocytes predominantly proliferate due to local signals at the blood vessel interface after injury (see, e.g., Sirko et al., 2013), or may already differ from other astrocytes prior to injury. For example, different electrophysiological properties may predispose juxtavascular astrocytes to more readily resume proliferation, for example, due to lower $K_{ir}4.1$ levels or a more depolarized resting membrane potential. Moreover, using the StarTrack method (Bribian, Figueres-Onate, Martin-Lopez, & Lopez-Mascaraque, 2016; Figueres-Onate, Garcia-Marques, & Lopez-Mascaraque, 2016; Garcia-Marques & Lopez-Mascaraque, 2013), we revealed that both juxtavascular and non-juxtavascular astrocyte clones derive from distinct single progenitor cells. However, to which extent these distinct clones may differ in their ion channel composition, and how this may relate to their reaction after injury, remains unexplored. Indeed, despite the importance of juxtavascular astrocytes in the injury context, their electrophysiological properties have never been examined. These data prompted us to characterize the electrophysiological properties of juxtavascular versus non-juxtavascular astrocytes in acute slice preparations of murine cerebral cortex prior to and after TBI.

2 | MATERIALS AND METHODS

2.1 | Mouse strain

Experiments were performed on BAC Aldh1l1-eGFP mice (Tg (Aldh1l1-EGFP)OFC789Gsat/Mmucd; Gensat Project; Heintz, 2004) maintained on FVB/N background of both sexes. The green fluorescent protein (GFP) is expressed in nearly all astrocytes in the adult CNS driven by the regulatory elements of the aldehyde dehydrogenase 1 family member L1 (Aldh1l1) in this mouse line (Heintz, 2004). The experimental animals were housed and bred in an open Type II cage system in groups of no more than eight animals and were provided with changing enrichment. The animals were provided with food and water ad libitum and all conditions were in accordance with the RL2010/63/EU. All experiments were in accordance with and approved according to the German "Tierschutzgesetz."

2.2 | Stab wound lesion

Surgical procedures were approved by the government of upper Bavaria (Gz.: 55.2-1-54-2532-76-2016). The experimental animals were briefly anesthetized with 100% isoflurane (IsoFlo®; Zoetis Schweiz GmbH) until the righting reflex was lost and then put under general anesthesia with an intraperitoneal injection (i.p.) of 0.5 mg/kg medetomidine (Oreon Pharma; Domitor 1 mg/ml), 5 mg/kg midazolam (Braun GmbH; 5 mg/ml) and 0.05 mg/kg fentanyl (Jannsen Pharmaceutica; 0.05 mg/ml). Then, they were head fixed in a motorized stereotaxic drive (NeuroStar GmbH) and put onto a feedback controlled heating pad (Physitemp Instruments; TCAT-2DF controller and F040070504b 12 V/5.3 Ω/1408C-01 pad) set to 36°C. A craniotomy was performed and a lancet was inserted 0.6 mm deep into the somatosensory cortex 1.5–2.5 mm parasagittal to the midline and then moved several times 1–1.5 mm caudally through the brain to introduce a stab wound lesion. After removing the lancet from the brain, the cranial window was closed with the small piece of skull, which was removed earlier in the procedure. Thereafter, we closed the operating area with a suture using surgical suture material (Feuerstein GmbH; Seide Schwarz 45 cm USP 4/0 (m 1.5) HS 18). To

antagonize the anesthesia, the animals were injected i.p. with 2.5 mg/kg atipamezole (CP Pharma; Revertor 5 mg/ml), 0.5 mg/kg flumazenil (Hexal AG; 0.5 mg/ml), and 0.1 mg/kg buprenorphine (Bayer AG; Buprenorvet 0.3 mg/ml). During the whole procedure, the animals were provided with dampened oxygen (Linde Gas Therapeutics GmbH; Conoxia ® GO₂X) through a breathing mask to facilitate breathing and guarantee proper ventilation.

2.3 | Immunohistochemistry

Animals (P36-65) were injected i.p. with a lethal dose of Narcoren (400–800 mg/kg; Merial GmbH; pentobarbital sodium 16 g/ml). For post-mortem transcardial perfusion, Ringer solution containing 0.1% heparin (Meditech Vertriebs GmbH) was used for 5 min followed by a solution containing 4% PFA in 0.05 M PBS (pH 7.4) for 20 min. Subsequently, the brain was removed from the skull and post-fixed for 2 hr in 4% PFA solution at room temperature on a shaker. Brains were incubated three times for 10–15 min in 0.02 M PBS on the shaker and then embedded in 4% agar (Meditech Vertriebs GmbH). Coronal sections of the somatosensory cortex were cut 30 μm thick with a VT 1200S vibratome (Leica Microsysteme Vertrieb GmbH) and rinsed in 0.02 M PBS. First, the slices were incubated for 20 min in blocking solution (1% bovine serum albumin, 0.1% saponin, 0.5% TritonX100, 0.02 M PBS) to prevent unspecific antibody binding. Then, this solution was replaced with new blocking solution that additionally contained primary antibodies to $K_{ir}4.1$ (rabbit; 1:200; Alomone Labs APC-035), $K_V4.3$ (rabbit; 1:200; Alomone Labs APC-017), Ki67 (rat; 1:100; ThermoFisher 14-5698-82), GFAP (mouse; 1:500; Sigma G3893), and GFP (chicken; 1:500; Aves Labs GFP-1020) and slices were incubated 48 hr at 4°C. Thereafter, slices were washed three times for 15–20 min in washing solution (0.02 M PBS with 0.1% saponin and 0.5% Triton X100) and then incubated with secondary antibodies to mouse AMCA (donkey; 1:100; Dianova 715-156-150), to chicken Alexa488 (donkey; 1:300; Dianova 703-546-155), to rabbit Cy3 (donkey; 1:400; Dianova 711-165-152), and to rat DyLight594 (donkey; 1:200; Dianova 711-516-152) diluted in blocking solution over night at 4°C. For blood vessel labeling DyLight 649-coupled *Lycopersicon esculentum* (tomato) lectin (TL 649; 1:250; Vector Laboratories DL-1178) was added. The next day, slices were washed three times for 15–20 min in washing solution at room temperature. For nuclear labeling, sections were incubated for 20 min in DAPI solution (1:1000; Thermo Fisher; 62248). After washing for 5 min, slices were put onto slides, which were mounted with VECTASHIELD Antifade Mounting Medium (Vector Laboratories) and cover slips and sealed with clear nail polish.

2.4 | Slice preparation for electrophysiology

For electrophysiological recordings, control mice (P24-38) were anesthetized with 100% isoflurane (IsoFlo®; Zoetis Schweiz GmbH) and quickly decapitated under anesthesia. For blood vessel labeling in animals with a stab wound lesion (P27-50), they were first quickly anesthetized with Isoflurane (IsoFlo®, 100% isoflurane; Zoetis Schweiz

GmbH), then MMF was injected i.p. (see above), followed by tail vein (i.v.) injection of 50 μL Texas Red® labeled dextran (Molecular Probes Inc.; 70,000 g/mol; 10 mg/ml in NaCl). After 10–15 min incubation, the animals were decapitated. The brains of all experimental animals were dissected from the skull and placed in ice-cold carbonated artificial cerebrospinal fluid (ACSF) slice solution containing 120 mM sucrose, 25 mM NaCl, 25 mM NaHCO₃, 2.5 mM KCl, 1.25 mM NaH₂PO₄, 3 mM MgCl₂, 0.1 mM CaCl₂, 25 mM glucose, 0.4 mM ascorbic acid, 3 mM myo-Inositol, and 2 mM Na-pyruvate (pH 7.4 by bubbling with 95% O₂ and 5% CO₂). The 200-μm-thick coronal brain sections were cut with a Leica VT1200S vibratome (Leica Microsysteme Vertrieb GmbH). The tissue slices were then transferred to a beaker filled with ACSF patch solution containing 125 mM NaCl, 25 mM NaHCO₃, 2.5 mM KCl, 1.25 mM NaH₂PO₄, 2 mM CaCl₂, 1 mM MgCl₂, 25 mM glucose, 0.4 mM ascorbic acid, 3 mM myo-Inositol, and 2 mM Na-pyruvate (pH 7.4 by bubbling with 95% O₂ and 5% CO₂). The beaker was placed into a water bath heated to 36°C and slices were incubated for 45 min while being continuously bubbled with 95% O₂ and 5% CO₂. Subsequently, the slices were stored at room temperature and used for electrophysiological experiments after they had rested for at least 20 min.

2.5 | Electrophysiology

To perform electrophysiological recordings, the slices were transferred into a recording chamber in an Olympus BX51WI microscope (Olympus Europa Holding GmbH) equipped with a light source (Olympus TH4-200; Olympus Europa Holding GmbH) and an infrared filter for bright field microscopy and a white light source (LEj GmbH) for fluorescent imaging. An Orca-R² Digital Camera C10600 with the corresponding Hokawo software (Hamamatsu Photonics K.K) was installed and Olympus objectives with a 4× (Plan N 0.1; Olympus Europa Holding GmbH) and a 60× (PlanFL N 1.0; Olympus Europa Holding GmbH) magnification were used. To guarantee the health of the slices, the recording chamber was constantly perfused with freshly carbonated ACSF patch solution. All the electrophysiological recordings were performed at room temperature. For voltage-clamp whole-cell recordings, borosilicate glass capillaries (BM150F-10P with filaments, 1.5 mm OD/0.86 mm ID/100 mm L; BioMedical Instruments) with a resistance between 3.5 and 5.5 MΩ when filled with intracellular solution containing 130 mM K-gluconate, 20 mM HEPES, 10 mM EGTA, 13 mM Na₂-ATP, and 1 mM MgCl₂ (osmolarity: 290 ± 2 mOsm; pH 7.25–7.28 that was achieved via titration with either 1 M NaOH or 1 M KOH) were used. The recordings were performed with a double patch clamp EPC 10 *USB* amplifier (HEKA Elektronik Dr. Schulz GmbH). Astrocytes were identified by fluorescent labeling with GFP and their location toward blood vessels was either identified by bright field microscopy or by fluorescent blood vessel labeling (Texas Red® labeled dextran or TL 649). TL 649 labeled blood vessels only at the slice surface in electrophysiological experiments, because incubation times were too short compared to immunohistochemistry, where also deeper blood vessels were stained. We have thoroughly scanned the

regions below and above the focal plane of the astrocyte using bright field microscopy and switched several times between bright field and epifluorescence to avoid a wrong assignment of astrocytes. In the slices from animals with a lesion, the fluorescent labeling of blood vessels allowed the unambiguous classification. For the identification, a dual band GFP/mCherry ET Filterset was used (F56-019; AHF Analysentechnik AG). The capacitive artifact (C-fast) of the recording electrode was compensated in all recordings. All obtained data were corrected for a liquid junction potential of −16 mV. Data were acquired with a sampling rate of 20 kHz and Bessel filtered at 2.9 and 10 kHz. The recording protocols were created with the help of the pulse generator in the PatchMaster software (HEKA Elektronik Dr. Schulz GmbH). The astrocytes were clamped to the V_r measured in current-clamp mode and subsequently injected with 200-ms-long voltage steps ranging from −176 to +174 mV in 10 mV increments to obtain the current response from the patched cell for passive electrophysiological parameter identification. For all further analysis, only cells that showed stable recordings and constant parameters were taken into account.

In the experiments performed on control animals (P24-38) for pharmacological identification of $K_{ir}4.1$ channels, astrocytes were clamped to their V_r measured in current-clamp mode and subsequently injected with 200-ms-long voltage steps ranging from −176 to +174 mV in 10 mV increments to obtain the current response. Afterward, the $K_{ir}4.1$ channel blocker $BaCl_2$ dihydrate (200 μM; 31125-500G-R; Sigma Aldrich Chemie GmbH) diluted in recording solution was washed into the recording chamber for 10 min.

2.6 | Clonal analyses: StarTrack method

Clonal analysis was performed with the StarTrack approach (Figueres-Onate et al., 2016; Garcia-Marques & Lopez-Mascaraque, 2013). Briefly, StarTrack is based on the genomic incorporation of 12 plasmids encoding six different fluorescent reporter proteins, localized cytoplasm or nucleus, under the GFAP promoter. To allow the genomic integration of these constructs, each plasmid incorporates inverted terminal repeat sequences recognized by the piggyBac transposase plasmid. This results in a unique color combination code detecting glial clones derived from single progenitors. This will allow following cell dispersion of the progeny from embryonic mice single progenitor cells and generated an inheritable mark in astrocyte lineages.

Wild type C57BL/6 mice from the Cajal Institute animal facility were treated according to the European Union guidelines on the use and welfare of experimental animals (2010/63/EU) and those of the Spanish Ministry of Agriculture (RD 1201/2005 and L32/2007). The CSIC Bioethical Committee approved all the procedures (PROEX 44/14). The day when vaginal plug was detected was referred to as E0 and day of birth as postnatal day (P) 0. In utero electroporation was performed as previously described (Garcia-Marques & Lopez-Mascaraque, 2013). Briefly, E14 pregnant mice were deeply anesthetized by isoflurane inhalation and uterine horns were exposed by

laparotomy. Embryos were visualized by trans-illumination and StarTrack plasmid mixture was injected into the lateral ventricle of each embryo. Next, one or two trains of five square wave pulses (35 V; 50 ms followed by 950 ms intervals) were delivered on each embryo. Uterine horns were placed back into abdominal cavity. Injected embryos were allowed to develop normally until birth. Brains were examined at P35 after transcardially perfusion with PBS plus heparin (5 min) followed by 4% PFA (20 min) and 2 hr post fixation. Brain vibratome slices (50 μm) were processed for $K_v4.3$ (rabbit; 1:200; Alomone Labs APC-017) and $K_{ir}4.1$ (rabbit; 1:200; Alomone Labs APC-035), incubated with secondary Alexa633 anti-rabbit 1:1000. Images at 40× were acquired on a Leica TCS-SP5 confocal microscope, collecting the different fluorescent proteins in separate channels. The wavelength of excitation (Ex) and emission (Em) for each XFP were (in nanometers, nm): mT-Sapphire (Ex: 405; Em: 520–535), mCerulean (Ex: 458; Em: 468–480), EGFP (Ex: 488; Em: 498–510), YFP (Ex: 514; Em: 525–535), mKO (Ex: 514; Em: 560–580), mCherry (Ex: 561; Em: 601–620), and Alexa 633 (Ex: 633; Em: 650–760). Maximum projection images were created using confocal (LASX Leica).

2.7 | Microscopy

Images were acquired with a Leica TCS SP-5 confocal laser scanning microscope (Leica Microsystems Vertrieb GmbH) using either a HCX PL APO Lambda Blue 20× 0.7 immersion objective or a HCX PL APO Lambda Blue 63× 1.4 oil immersion objective. The virtual slices were set constantly to 0.5 μm z-step size and an image size of 512 × 512 pixels. The bidirectional scanning mode was chosen and laser scanning frequency varied between 400 and 1,000 Hz depending on the zoom factor for the corresponding picture. The line average was calculated from three subsequent line scans and the size of the pinhole was automatically adjusted by the software. The microscope used the following lasers: a diode laser (405 nm; 25 mW), an argon laser (458, 467, 488, and 514 nm; 5 mW), a DPSS laser (561 nm; 10 mW), a HeNe laser (594 nm; 2.5 mW), and another HeNe laser (633 nm; 10 mW) to visualize the different fluorescence labels. Before scanning, the laser power and the gain were adjusted to ensure an optimal fluorescence signal.

2.8 | Data analysis

Electrophysiological data acquired with the PatchMaster software (HEKA Elektronik Dr. Schulz GmbH) were loaded into the IGOR PRO 6.35A software (WaveMetrics Inc.) with the help of the Patchers Power Tools 2.19 extension (Dr. Francisco Mendez and Frank Würrihausen; Max-Planck-Institut für biophysikalische Chemie Göttingen). The raw current traces were further analyzed with custom written IGOR PRO procedures.

GrapPad Prism 7.05 (GraphPad Software) was used to further process data, to perform statistical analysis on electrophysiological data, cell-counting analysis, and for graph design. Data sets for V_r and

G_r passed D'Agostino–Pearson normality test. Therefore, Gaussian distribution was assumed and the results were presented as the mean ± SD. For comparison of passive electrophysiological properties, we determined statistical significance by one-way ANOVA or t-tests. In case of significance, one-way ANOVA was followed by Tukey's multiple comparisons test. To check for differences in the number of astrocytes that possess certain features with the help of contingency analysis, a two-sided Fisher's exact test was used. In case of experiments, in which cellular parameters were compared before and after application of an ion channel blocker, the paired t-test was used.

The categorization into passive and non-passive astrocytes was based on a linear regression of their steady-state current–voltage (IV) relationship. Astrocytes were identified as non-passive if R^2 of the linear regression was less than 0.9987 (Kafitz, Meier, Stephan, & Rose, 2008).

All images acquired with the Leica TCS SP-5 confocal laser scanning microscope (Leica Microsysteme Vertrieb GmbH) were further processed and analyzed with ImageJ software (Wayan Rasband, National Institutes of Health). Image Stacks were corrected for a z chromatic shift between color channels. For cell counting, we used the ImageJ manual counting tool and analyzed all optical sections of a stack individually. Images were produced by making z-stack maximum projections of a certain number of optical sections and brightness and contrast was adjusted for optimal signal to noise ratio. In all statistical tests, the significance level was set at $p < .05$.

3 | RESULTS

3.1 | Juxtavascular and non-juxtavascular astrocytes share similar electrophysiological properties in the somatosensory cortex of Aldh1l1-GFP mice

We first focused on basic electrophysiological properties of astrocytes to find out whether there exists an inherent difference between juxtavascular and non-juxtavascular astrocytes. To readily detect astrocytes, we used BAC Aldh1l1-eGFP transgenic mice (Heintz, 2004) to carry out whole-cell patch-clamp recordings in acute slices of the somatosensory cortex. To detect GFP$^+$ astrocytes (Figure 1a–i) at juxtavascular positions we incubated slices with DyLight 649-coupled Lycopersicon esculentum (tomato) lectin (TL 649) to label blood vessels. Comparison to acute slices without fluorescent blood vessel labeling showed that juxtavascular astrocytes could also be reliably detected with bright field microscopy, because somata of juxtavascular astrocytes are directly adjacent to blood vessels (Figure 1c,d, cyan arrow) and their green fluorescent processes often enwrap larger blood vessels (Figure 1c, red arrows). The resting membrane potential (V_r) and the resting membrane conductance (G_r) were determined from steady-state current–voltage (IV) relationships measured in voltage-clamp mode (Figure 1j–l). Values of V_r showed a pronounced heterogeneity, but no significant difference between the respective subgroups (means ± SD: −84.6 ± 7.9 mV [non-juxta] vs. −85.0 ± 9.9 mV [juxta]; t-test: $p = .8450$). We observed a similarly

high heterogeneity for G_r, with juxtavascular astrocytes showing 20% larger G_r (means ± SD: 72.2 ± 29.0 nS [non-juxta] vs. 87.5 ± 27.6 nS; t-test: $p = .0284$). There was no correlation between V_r or G_r and the animals' age (Figure S1). A major fraction of the current appeared to be carried by the inwardly rectifying $K_{ir}4.1$ potassium channel, as Ba^{2+} (200 μM) reduced the whole-cell currents (Figure S2).

Different astrocyte subtypes can be distinguished by comparing IV relationship, based on their electrophysiological properties (Figure 1j–l). The majority of astrocytes showed a typical Ohmic passive current pattern (81% of juxtavascular and 70% of non-juxtavascular astrocytes; Figure 1j,l), while smaller subsets of astrocytes exhibited non-passive current patterns (Figure 1k) with non-linear IV relationships (Figure 1l). There was no difference between the two astrocyte subgroups regarding the relative frequency of the two current patterns under control conditions (Fisher's-exact test: $p = .0996$; Figure S3). The V_r of astrocytes in the different subgroups was equal (Figure 1m; one-way ANOVA: $p = .2544$). The differences observed for G_r (Figure 1n; one-way ANOVA: $p = .0051$; Table S1) reflect the classification into passive and non-passive astrocytes based on their IV relationship. Overall juxtavascular astrocytes share the electrophysiological characteristics of a K$^+$-dominated V_r and passive current patterns with other parenchymal astrocytes.

3.2 | Clonal heterogeneity in K$^+$ channel expression in astroglia in the cerebral cortex grey matter

Next, we used immunohistochemistry to explore possible differences in expression of specific K$^+$ channels between astrocyte subsets. Immunostaining was combined with blood vessel labeling using TL 649 as described above to distinguish juxtavascular from non-juxtavascular astrocytes. Both juxtavascular and non-juxtavascular astrocytes in the somatosensory cortex were $K_{ir}4.1$-immunopositive (Figure 2). $K_{ir}4.1$ immunoreactivity was detected only in astrocytes, not in neurons, and revealed no heterogeneity as more than 95% of the astrocytes were immunopositive across all layers (one-way ANOVA: $p = .4291$; Figure 2i).

Next, we stained for $K_v4.3$ known to be expressed in astrocytes (Bekar et al., 2005). Interestingly, $K_v4.3$ immunoreactivity was heterogeneous with most astrocytes positive, but some with much lower $K_v4.3$ signal (Figure 3; blue vs. white arrows in e–h). This prompted us to ask if astrocytes originating from a common ancestor may share expression of this channel. To examine the clonal origin of $K_v4.3^{\pm}$ astrocytes, we used the StarTrack method based on in-utero electroporation of constructs containing a panel of fluorescent proteins directed to astrocyte expression by the GFAP-promoter (see Section 2). This method had previously revealed astrocyte clones (labeled by the same fluorescent combination and hence originating from the same progenitor cell) comprising only juxtavascular astrocytes (Bribian et al., 2016; Garcia-Marques & Lopez-Mascaraque, 2013). After targeting progenitor cells with StarTrack, we found no heterogeneity for astrocyte clones with regard to $K_{ir}4.1$ as expected (Figure S4).
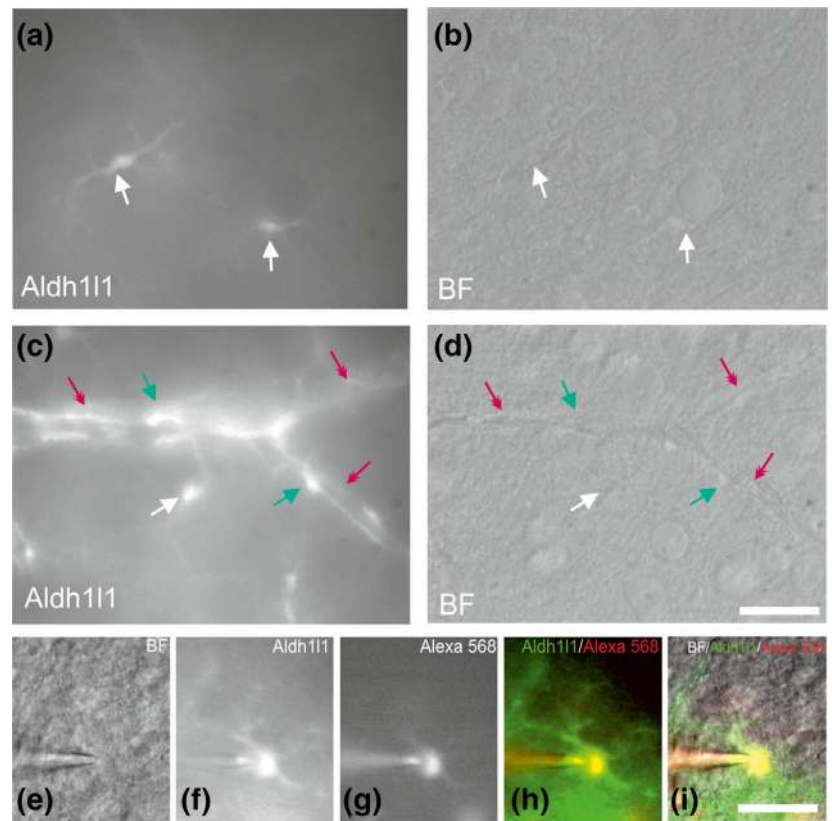
FIGURE 1 Electrophysiological characterization of juxtavascular and non-juxtavascular astrocytes. (a–d) Example pictures of fluorescent Aldh1l1-eGFP-positive astrocytes (left pictures) and corresponding bright field (BF) images (right pictures) in 200-μm-thick coronal sections. The white arrows mark non-juxtavascular astrocytes. Red arrows point to blood vessels, which were identified either via eGFP fluorescence resulting from astrocytic processes excessively enwrapping them or in the BF picture mode. Cyan arrows point to juxtavascular astrocytes that have their cell somata directly adjacent to blood vessels. Scale bar: 23 μm. (e–i) Close-up pictures of a non-juxtavascular astrocyte ([e] BF; [f] Aldh1l1-eGFP fluorescence) being patched with a borosilicate glass electrode. The electrode is filled with intracellular solution and Alexa 568 fluorescent dye to visualize the patched cell (Alexa 568, g). Pictures (h) and (i) show overlays of the different single channels to proof that the patched cell is really the eGFP positive astrocyte (yellow). Scale bar: 45 μm. (j–l) Astrocytes can be classified according to their current response patterns into passive and non-passive ones. (j, k) Example current responses to 200-ms long voltage steps, ranging from −176 to +174 mV in 10 mV increments, are shown for passive (j) and non-passive (k) astrocytes. (l) Corresponding steady state IV relationships (norm I_{steady}, normalized steady-state current) for the two astrocytes displayed in j (blue, linear regression) and k (red) (m, n) Comparison of passive electrophysiological properties (V_r, G_r) of non-juxtavascular (circles; $n = 43$) and juxtavascular astrocytes (squares; $n = 31$) of the healthy somatosensory cortex. The cells were classified as passive (blue) and non-passive (red) based on their IV relationship. The means of V_r (± SD) did not differ significantly (m; one-way ANOVA, $p = .2544$), whereas for G_r values (means ± SD), two groups showed a significant difference (n; one-way ANOVA, $p = .0051$; Tukey's multiple comparisons test, $p = .0024$)
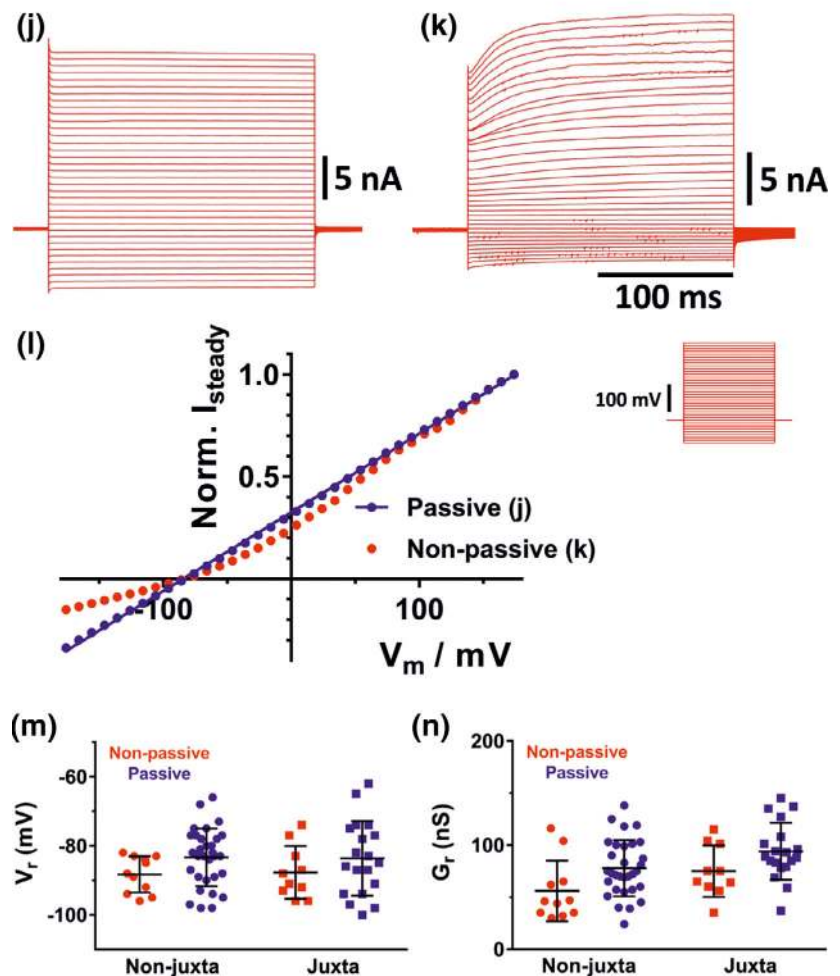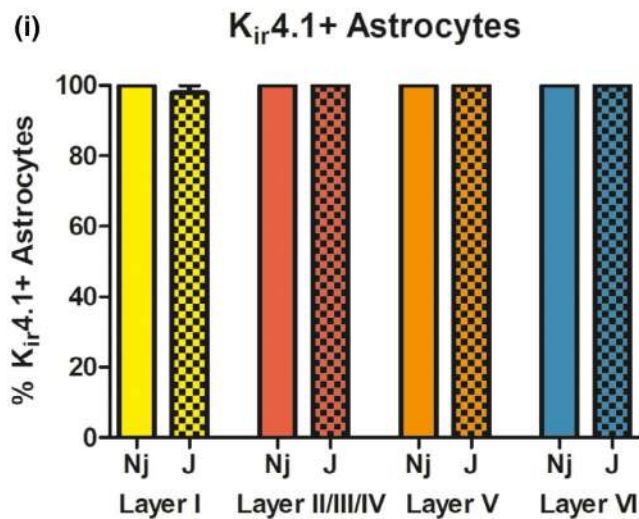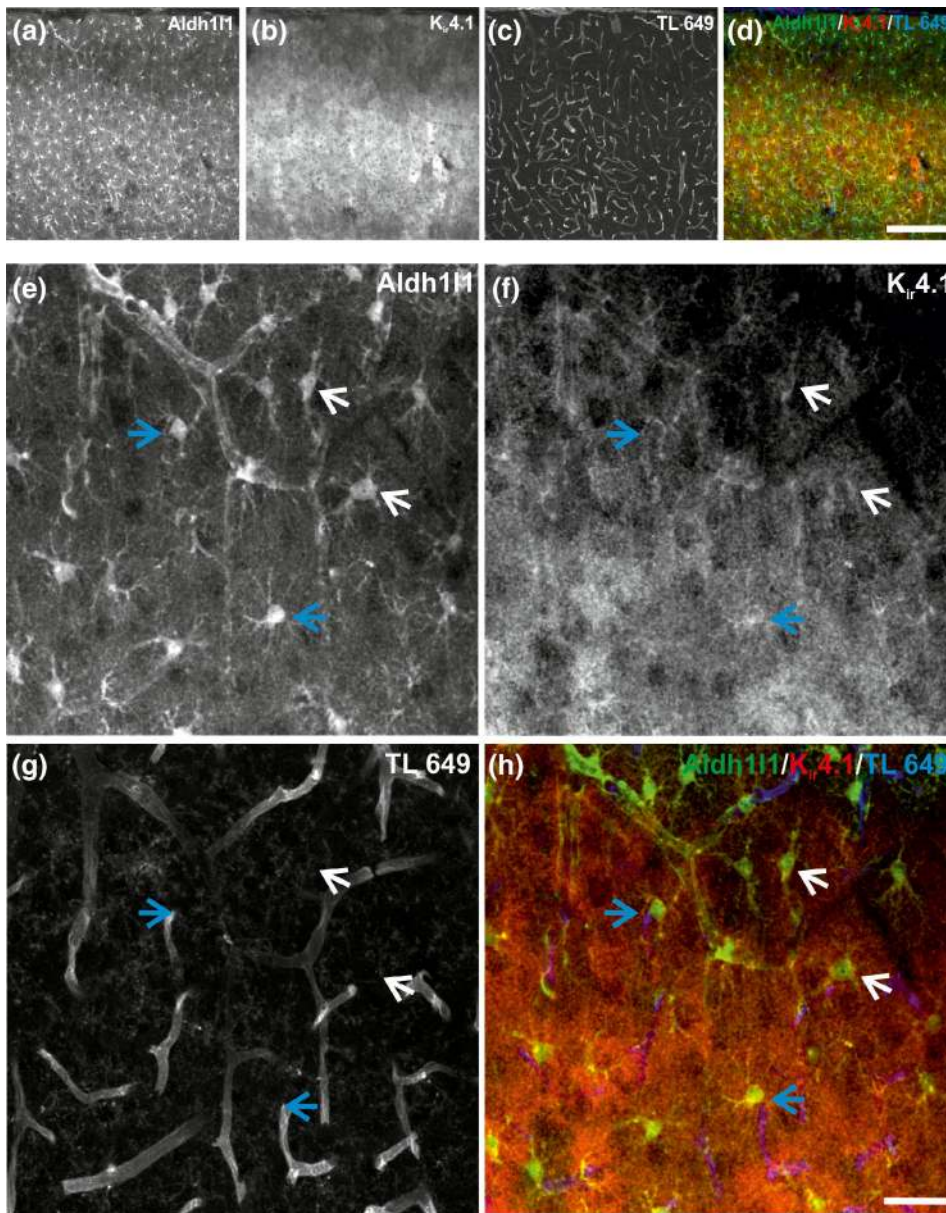
FIGURE 2 Immunohistochemistry suggests homogeneous expression of the inwardly rectifying $K_{ir}4.1$ channel in astrocytes. (a–d) Maximum z-projection of a control hemisphere (P51) (a), $K_{ir}4.1$ staining (b), blood vessels visualized with TL 649 (c), as well as an overlay of the three channels (d). All astrocytes are positive for $K_{ir}4.1$. Scale bar: 215 μm. (e–h) Maximum z-projection of a close-up of layer II/III/IV (same slice as in [a]). The white arrows indicate $K_{ir}4.1$-positive non-juxtavascular astrocytes and blue arrows point to $K_{ir}4.1$-positive juxtavascular astrocytes. Scale bar: 35 μm. (i) $K_{ir}4.1$ is homogenously expressed in astrocytes across all layers (one-way ANOVA, $p = .4291$) as analyzed by counting of $K_{ir}4.1$-positive astrocytes (P40-51; $n = 3$). The graph shows the percentage of $K_{ir}4.1$-positive astrocytes. J, juxtavascular, Nj, non-juxtavascular
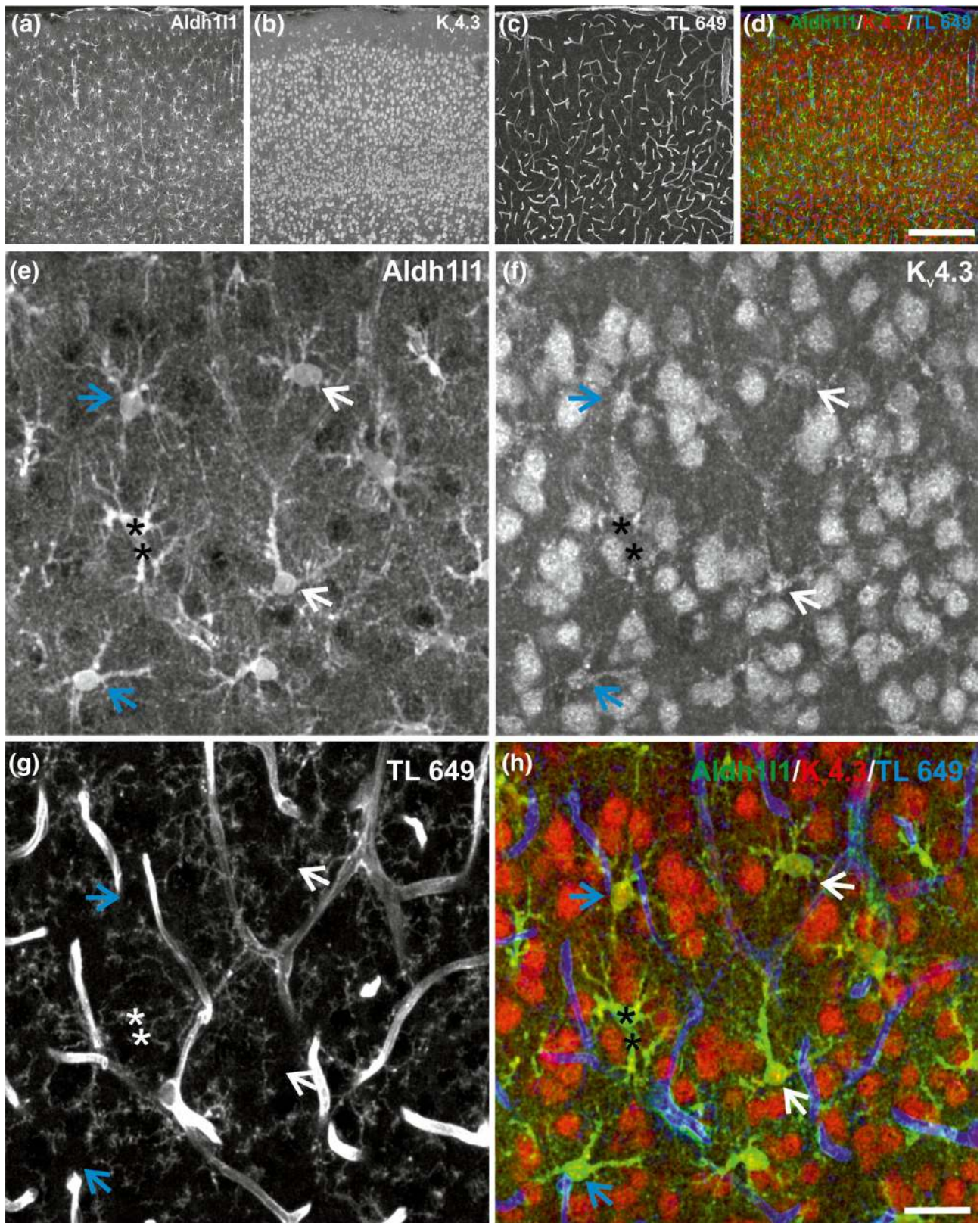
FIGURE 3 Heterogeneous expression of $K_v4.3$. (a–d) Overview maximum z-projection (all confocal sections) of the somatosensory cortex in a control hemisphere (P51) (a), $K_v4.3$ staining (b), blood vessels visualized with TL 649 (c), and an overlay of these three channels (d). Scale bar: 215 μm. (e–h) Maximum z-projection of a close-up of layer II/III/IV (same slice as in [a]). $K_v4.3$-positive astrocytes are marked by white arrows (non-juxtavascular) and by blue arrows (juxtavascular), respectively, whereas $K_v4.3$-negative astrocytes are labeled with an asterisk. Scale bar: 26 μm
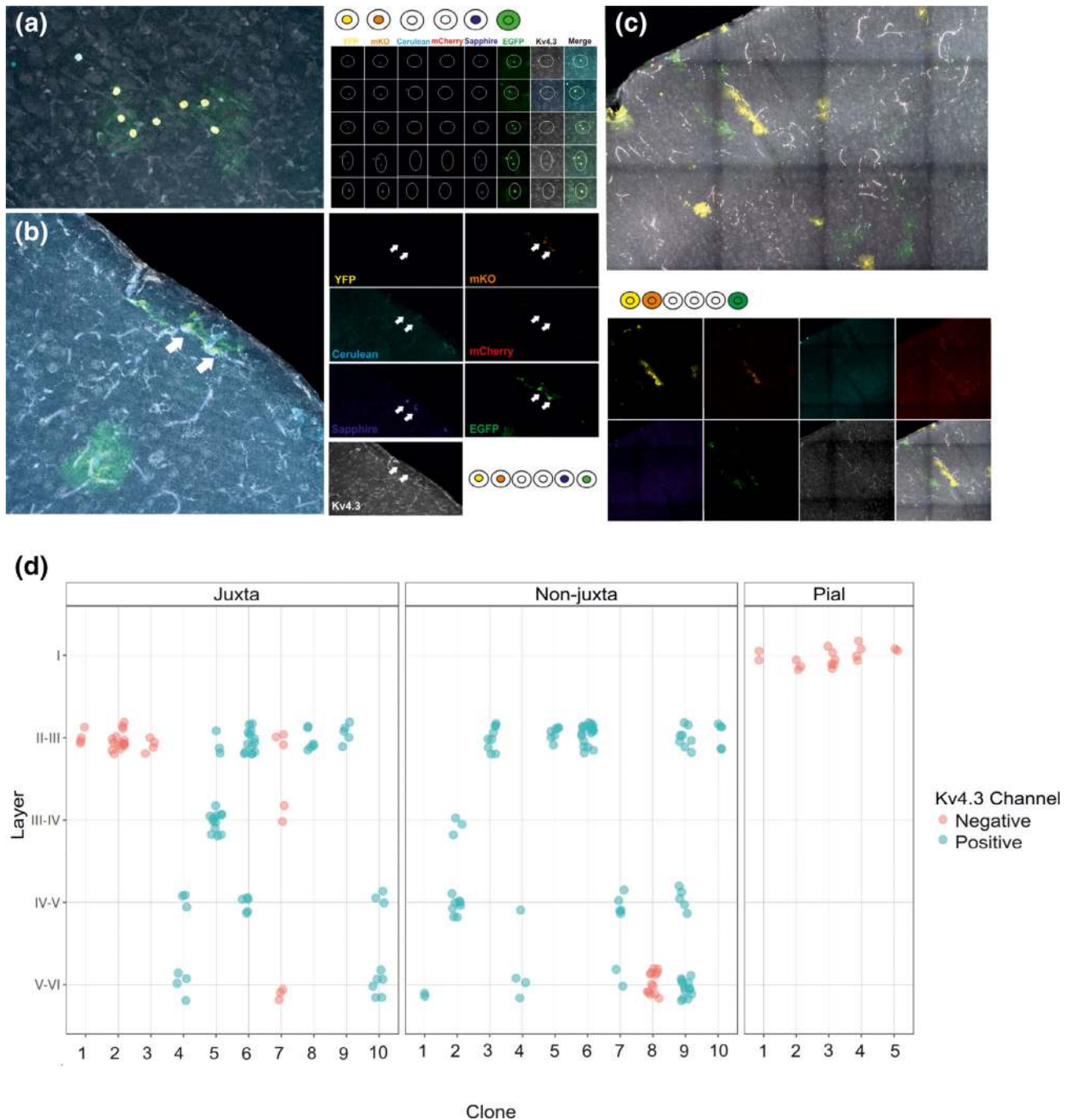
FIGURE 4 Clonally related cells positive for K$_v$4.3. (a) K$_v$4.3 positive astrocytes form a non-juxtavascular clone at P35 after in utero electroporation (E14) with StarTrack. Sibling cells are labeled with the same fluorescent color codes. (b) StarTrack labeled pial clone, with none cells positive for K$_v$4.3. (c) Representative juxtavascular clone with sibling cells negative for K$_v$4.3. In the three images, clonally related cells displayed the same fluorophores and K$_v$4.3 expression. (d) The graphs show the dispersion within the cortex of astrocyte StarTrack labeled clones and their K$_v$4.3 expression

Conversely, the expression of K$_v$4.3 in StarTrack-labeled cells revealed a K$_v$4.3 heterogeneity depending on the ontogenic origin, since all members of a clone were either positive or negative for K$_v$4.3 (Figure 4). In relation to the clonal cell dispersion, the vast majority (80%) of clones negative for K$_v$4.3 ($n = 10$) were found in superficial layers or at sub-pial positions (Figure 4b,c), and almost all (90%) were exclusively composed of juxtavascular astrocytes (Figure 4c). Notably,

not a single sibling cell of pial clones was positive for K$_v$4.3. However, sibling astrocytes belonging to non-juxtavascular clones were positive for K$_v$4.3, independently of their cortical layer location (Figure 4a,d, Video S1). These results demonstrated that in juxtavascular clones, the expression of K$_v$4.3 was clonally related in a layer-specific manner, with all the cells of the same clone either positive or negative for K$_v$4.3 (Figure 4d).

3.3 | Electrophysiological differences and K$_{ir}$4.1 down-regulation in astrocytes of the somatosensory cortex after TBI

Next, we determined the electrophysiological properties of these groups of astrocytes after brain injury by patch-clamp recordings of juxtavascular astrocytes using the previously established stab wound injury model proliferation (Bardehle et al., 2013; Frik et al., 2018). The lesion (0.6 mm deep, 1.0–1.5 mm long; Figure 5a) was placed in the somatosensory cortex of the animals (P27-50) and electrophysiological analysis was performed 5 days thereafter, at the peak of astrocyte proliferation (Frik et al., 2018; Sirko et al., 2013). In addition, we
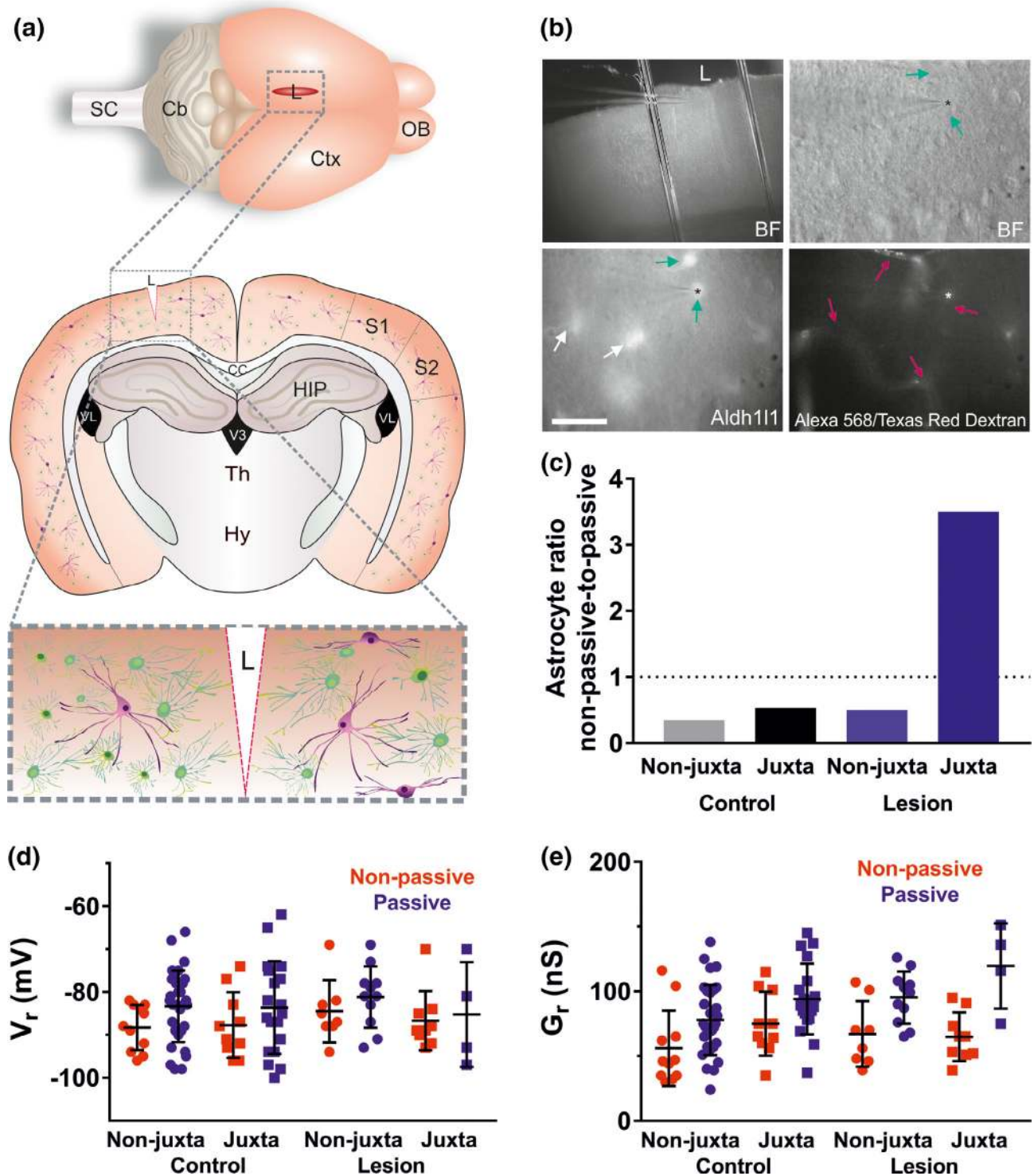

FIGURE 5 Legend on next page.

compared these results to data obtained from one animal at 1 dpi and one at 3 dpi, but did not obtain any significant differences to 5 dpi and, thus, included these data in our analysis (Figure S5). Whole-cell voltage-clamp recordings were performed on astrocytes of seven animals within a radius of 25–275 μm around the lesion that was easily identifiable with bright field microscopy (Figure 5b). Blood vessels were labeled with Texas Red-conjugated dextran via tail vein injection prior to decapitation to distinguish between juxtavascular and non-juxtavascular astrocytes (Figure 5b).

Interestingly, the ratio of non-passive to passive astrocytes rose significantly and reversed in juxtavascular ones (from 0.53 to 2.25 after injury) compared to non-juxtavascular astrocytes (from 0.35 to 0.73; Chi-Square test: $p = .0421$; Figure 5c). These data support the notion that juxtavascular astrocytes are particularly changed after injury. V_r values were not affected by TBI (Figure 5d; one-way ANOVA: $p = .9738$), while G_r exhibited significant differences between some groups (Figure 5e; one-way ANOVA: $p = .0001$; p values of post-test in Table S1). The only differences reflect the classification into passive and non-passive astrocytes based on their IV relationship, which most likely cause higher G_r values in passive than in respective non-passive astrocytes (only significant for juxtavascular ones after lesion, but visible as trend for the other groups). However, we did not observe systematic differences in G_r between control groups and the respective groups in lesioned animals (Figure 5e, Table S1). The heterogeneity of V_r and G_r values was substantial, but similar in all groups, as concluded from equal SD values (V_r: $p = .2084$ [Brown-Forsythe test], $p = .3152$ [Bartlett's test]; G_r: $p = .9683$ [Brown-Forsythe test], and $p = .8578$ [Bartlett's test]).

Given the changes observed in the ratio of non-passive to passive astrocytes (Figure 5c), we next asked, if the proliferating astrocytes may show differences in ion channel expression after brain injury. To do so, we double-stained for proliferating cells by Ki67 and the channel proteins at 5 dpi in combination with blood vessel labeling using TL 649 (Figure 6). As TL 649 also labels microglia cells in rodents, a high number of activated microglia can be seen at the lesion site.

$K_{ir}4.1$ immunoreactivity was much lower in reactive astrocytes after injury—consistent with previous analysis after injury (Gupta & Prasad, 2013; MacFarlane & Sontheimer, 1997; Olsen, Campbell, McFerrin, Floyd, & Sontheimer, 2010). Specifically, we observed that astrocytes proliferating at 5 dpi were often $K_{ir}4.1$-immune-negative (Figure 6f,g). The down-regulation of $K_{ir}4.1$ occurred preferentially in juxtavascular astrocytes (42% were $K_{ir}4.1$-negative; only 22% of non-juxtavascular astrocytes were $K_{ir}4.1$-negative). The significant difference in $K_{ir}4.1$ down-regulation between juxta- and non-juxtavascular astrocytes occurred in each animal (Figure 6h). In contrast, only 5% of Ki67-negative astrocytes ($n = 1,425$; 5 animals) were also negative for $K_{ir}4.1$, irrespective of whether they were juxtavascular or non-juxtavascular astrocytes (for both: fraction = 0.05 ± 0.01 [SEM]).

4 | DISCUSSION

We studied the potential role of ion channels and their influence on electrophysiological properties in astrocytic proliferation during post-traumatic processes in the somatosensory cortex of mice. As ion channel characteristics of juxtavascular astrocytes had so far not been examined specifically—neither in the intact nor in the injured brain—we focused on these groups of astrocytes. In the un-injured cortex, we did not detect any obvious differences in electrophysiological properties between the juxtavascular and the non-juxtavascular sub-population. However, following TBI, we observed a profound down-regulation of the major astrocytic ion channel, $K_{ir}4.1$, predominantly in juxtavascular astrocytes. In accordance with this change in $K_{ir}4.1$ expression, the ratio of juxtavascular astrocytes with non-passive to those with passive electrophysiological properties increased dramatically after a stab wound lesion. These findings support the concept that changes in electrophysiological properties accompany or govern a differential reaction of these astrocyte populations to injury. Intriguingly, clonal analysis revealing distinct ion channel composition of juxtavascular astrocytes in superficial cortex layers and at subpial

FIGURE 5 Electrophysiological characterization of juxtavascular and non-juxtavascular astrocytes after stab wound lesion. (a) Schematic of a mouse brain with a stab wound lesion (upper picture, encircled by dotted square). The middle picture shows a coronal section at the level of the lesion. The lower picture depicts a magnification. Neurons are shown in lilac, astrocytes in green. Astrocytes surrounding the lesion become reactive (dark green cell soma with light green nucleus), hypertrophic, and polarize toward the lesion. Astrocytes that are further away from the lesion are not activated (light green cell soma and dark green nucleus). SC: Spinal Cord; Cb: Cerebellum; Ctx: Cortex; OB: Olfactory Bulb; S1: Primary Somatosensory Cortex; S2: Secondary Somatosensory Cortex; HIP: Hippocampus; VL: Lateral Ventricle; V3: third Ventricle; Th: Thalamus; Hy: Hypothalamus; CC: Corpus Callosum; L: Lesion (Stab Wound). (b) Pictures show a 200-μm-thick coronal section of a lesioned (L) brain. The left upper picture shows a BF (bright field) overview (scale bar equals 504 μm) of the lesion (pink dotted line). Astrocytes surrounding the lesion within a radius of 25 to 275 μm were recorded. The other two lines are fibers of the grid. The right upper BF picture shows the same region magnified (scale bar: 29 μm). Astrocytes (cyan arrows) and the patch electrode are visible. The corresponding fluorescent Aldh1l1-eGFP-positive channel is shown in the left lower picture (juxtavascular astrocytes, cyan arrows; non-juxtavascular ones, white arrows). The white asterisk in the lower right picture indicates the patched astrocyte filled with Alexa 568 dye delivered through the patch pipette. Blood vessels were labeled with Texas Red dextran. (c) 71 control astrocytes (42 non-juxtavascular and 29 juxtavascular astrocytes) and 32 astrocytes from lesioned brains (19 non-juxtavascular and 13 juxtavascular) were sorted according to their current pattern. The ratio of non-passive to passive astrocytes was significantly higher and inverted after TBI. (d) Comparison of V_r of non-passive (red) and passive (blue) non-juxtavascular (circles) and juxtavascular astrocytes (squares) shows no significant difference in lesion and control brains (means ± SD; one-way ANOVA: $p = .9738$). (e) In contrast, G_r values are significantly different between some of the groups (means ± SD; one-way ANOVA, $p = .0001$) mainly reflecting the classification into passive and non-passive. The p values of a Tukey's multiple comparisons test are given in Table S1

FIGURE 6 Down-regulation of the inwardly rectifying $K_{ir}4.1$ channel in a fraction of proliferating non-juxtavascular astrocytes and juxtavascular astrocytes. (a–f) Confocal maximum z-projections (optical sections 1–27) of a lesioned hemisphere 5 dpi (P51). The four upper pictures show from left to right and up to down Aldh1l1-eGFP expressing astrocytes (a), $K_{ir}4.1$ staining (b), blood vessels and activated microglia visualized with TL 649 (c), and the proliferation marker Ki67 (d). (e) The left lower picture shows an overlay of Aldh1l1-eGFP positive astrocytes coded in green and the blood vessels and activated microglial cells in red. (f) The overlay shows Aldh1l1-eGFP-positive astrocytes (green), $K_{ir}4.1$ (red), and Ki67-positive nuclei (blue). Arrows indicate non-juxtavascular and juxtavascular non-proliferating astrocytes immunopositive for $K_{ir}4.1$. The dashed double arrows point to non-juxtavascular and juxtavascular astrocytes that are double positive for $K_{ir}4.1$ and Ki67. Proliferative (Ki67-positive), but $K_{ir}4.1$-negative astrocytes are marked with an asterisk. The dashed circle indicates the astrocytic domain of two proliferating astrocytes that are negative for $K_{ir}4.1$. Scale bar: 38 μm. (g) Ki67-positive non-juxtavascular and juxtavascular astrocytes were counted in five lesioned Aldh1l1-eGFP mice (P51-65) at 5 dpi. The majority of the proliferative astrocytes were $K_{ir}4.1$-postive. The difference between the two subclasses of astrocytes was a more pronounced $K_{ir}4.1$ down-regulation in proliferative, juxtavascular astrocytes compared to non-juxtavascular ones. (h) Analyzing these findings on the animal level revealed the statistical significance of the $K_{ir}4.1$ down-regulation in juxta-vascular astrocytes after TBI in comparison to the non-juxtavascular population (five animals; paired t test: $p = .0228$)
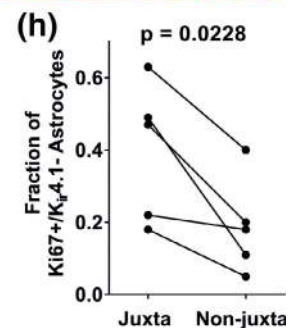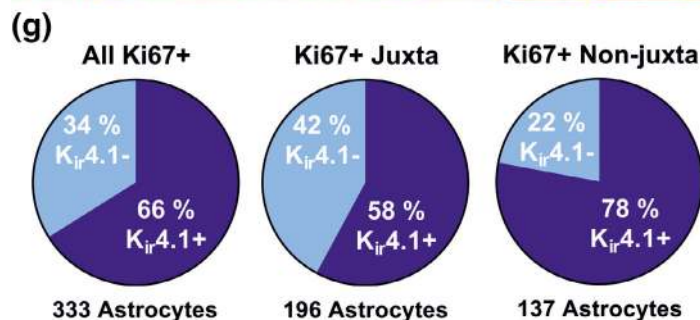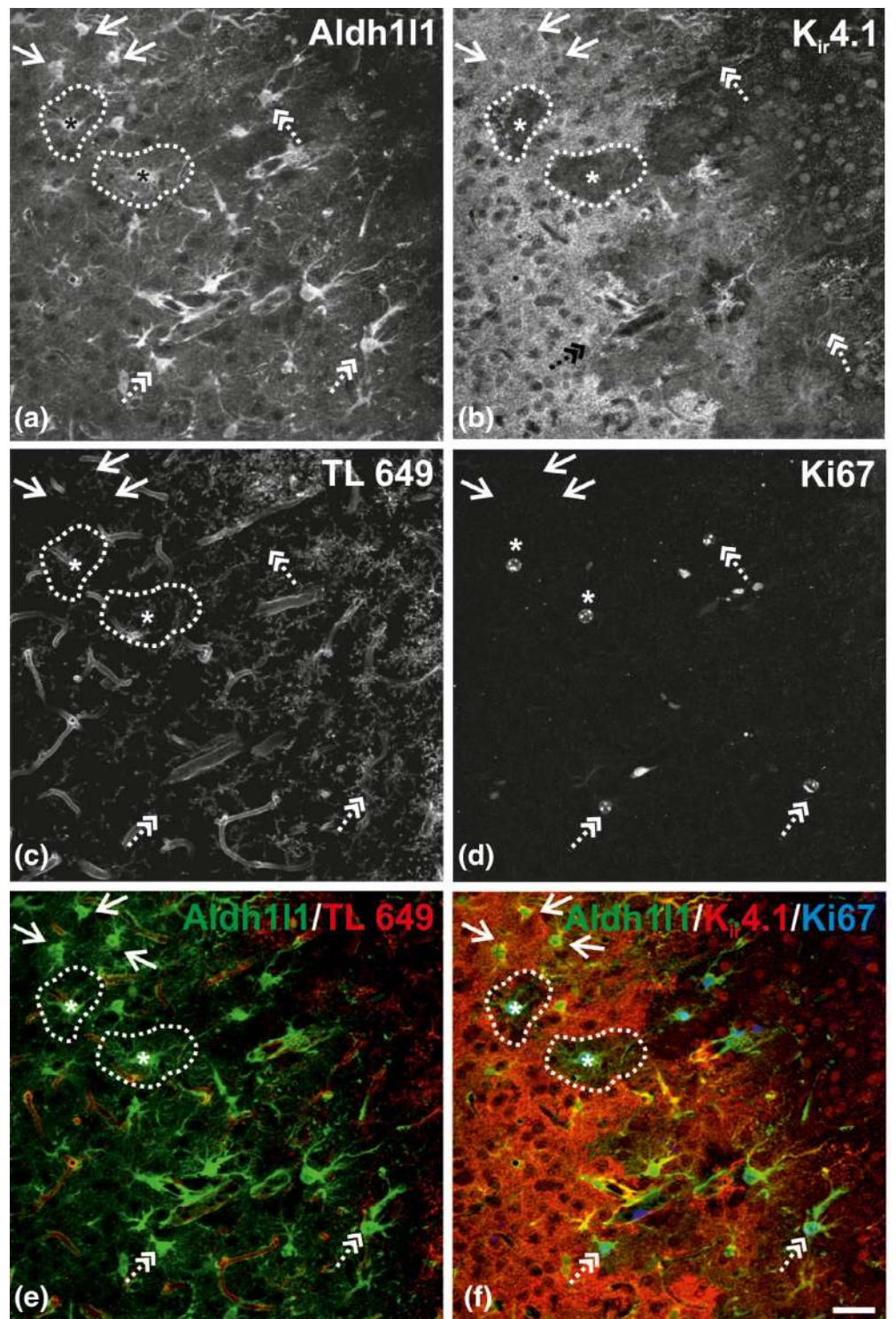
positions suggests not only a distinct regulation of such properties from the birth of the cells, but also implies certain preponderance of these cells to enact proliferation upon injury. This is based on the observation that proliferation is biased to superficial layers and juxtavascular astrocytes and $K_v4.3$ down-regulation in many astrocytes is already present in clones of superficial, juxtavascular astrocytes prior to injury.

A change in expression of some types of K^+ channels correlates with astrocytic proliferation in general and after traumatic events (Chvatal, Pastor, Mauch, Sykova, & Kettenmann, 1995; Honsa et al., 2014; MacFarlane & Sontheimer, 1997, 2000; Seifert et al., 2009). Based upon these facts as well as the dominance of $K_{ir}4.1$ in astrocytes, we tested the hypothesis that $K_{ir}4.1$ is a differentiator between non-juxtavascular and juxtavascular astrocytes regarding their distinct proliferative potential in response to TBI (Bardehle et al., 2013). We found $K_{ir}4.1$-immunopositivity in all astrocytes of healthy control brains; however, 5 days after infliction of a stab wound lesion, we found $K_{ir}4.1$ down-regulation predominantly in juxtavascular astrocytes in most animals more than double the fraction of proliferating juxtavascular astrocytes was negative for $K_{ir}4.1$ compared to the non-vascular astrocytes. Down-regulation of $K_{ir}4.1$ expression in proliferating astrocytes and up-regulation in differentiated cells was reported in other systems (Higashimori & Sontheimer, 2007; MacFarlane & Sontheimer, 1997, 2000; Olsen & Sontheimer, 2004), including reactive astrocytes after a lesion in rodents in vitro and in vivo (Gupta & Prasad, 2013; MacFarlane & Sontheimer, 1997; Olsen et al., 2010). However, this has never been discriminated for astrocyte subtypes. Interestingly, alteration of the $K_{ir}4.1$ expression level can also affect functions of neighboring neurons such as motor neuron activity in the intact spinal cord, but had no influence on neuronal survival even in disease conditions (ALS, Kelley et al., 2018). Thus, the bias to lose $K_{ir}4.1$ predominantly in juxtavascular astrocytes may not only favor their proliferation, but also influence neighboring neuron function.

To address the electrophysiological consequences upon injury, we investigated the IV relationships. In the healthy brain, we found typical passive current patterns with linear IV relationships that were reported to be dominant in mature astrocytes and mainly caused by channels such as the $K_{ir}4.1$ (Adermark & Lovinger, 2008; Djukic, Casper, Philpot, Chin, & McCarthy, 2007; Isokawa & McKhann, 2005; Kafitz et al., 2008; Moroni, Inverardi, Regondi, Pennacchio, & Frassoni, 2015; Seifert et al., 2009; Stephan & Friauf, 2014; Zhou, Schools, & Kimelberg, 2006). In accordance with our findings on $K_{ir}4.1$ down-regulation, TBI-induced reactivity of astrocytes resulted in a shift toward non-passive current responses especially in juxtavascular astrocytes with an increase in the ratio non-passive/passive from 0.53 to 2.25. Thus, also in electrophysiological properties, juxtavascular astrocytes are significantly different from their non-juxtavascular counterparts after injury. These changes suggest that reactive juxtavascular astrocytes are more often turning into a more immature state with non-passive current patterns. Thus, the heterogeneity of astrocytes already observed prior to injury, for example, by morphology and gene expression (Batiuk et al., 2020; Bayraktar et al., 2020; Cheng et al., 2019; Cragnolini, Montenegro, Friedman, &

Masco, 2018; Lanjakornsiripan et al., 2018; Magaki, Williams, & Vinters, 2018; Morel et al., 2017; Westergard & Rothstein, 2020), further increases after injury such that predominantly juxtavascular astrocytes show loss of $K_{ir}4.1$ immunostaining and non-passive properties.

Despite the $K_{ir}4.1$ down-regulation found in immunohistochemistry, we did not observe profound changes in V_r or G_r values (except for juxtavascular astrocytes in lesioned brains) after TBI. $K_{ir}4.1$ is known to stabilize V_r (Dallerac, Chever, & Rouach, 2013; Mishima & Hirase, 2010; Mishima, Sakatani, & Hirase, 2007) and V_r is crucial in cell-cycle progression (reviewed by Blackiston, McLaughlin, & Levin (2009) and Urrego, Tomczak, Zahed, Stuhmer, & Pardo (2014)). Accordingly, ischemia causes astrocyte depolarization (Honsa et al., 2014; Pivonkova, Benesova, Butenko, Chvatal, & Anderova, 2010). In scratch wound assays using rat spinal cord astrocyte cultures, proliferating astrocytes exhibited a reduction in G_r and depolarization attributed to $K_{ir}4.1$ down-regulation (MacFarlane & Sontheimer, 1997, 2000). Here, after stab wound injury, we observed a significant change in Gr within the juxtavascular astrocytes, namely between the passive and non-passive groups. Notably, however, up-regulation of other channel types, which contribute to passive current patterns (Adermark & Lovinger, 2008; Bordey & Sontheimer, 1997; Djukic et al., 2007; Isokawa & McKhann, 2005; Seifert et al., 2009) might mask the effect of $K_{ir}4.1$ loss.

Several studies have shown astrocytic gap junctional coupling and its influence on electrophysiological properties of individual astrocytes (Adermark & Lovinger, 2008; McKhann, D'Ambrosio, & Janigro, 1997; Meme, Vandecasteele, Giaume, & Venance, 2009), while others found an only minor contribution of gap junctional coupling to whole-cell current patterns (Du et al., 2015; Schools, Zhou, & Kimelberg, 2006). Here, we found no significant differences, but high variabilities in electrophysiological parameters between astrocyte subpopulations. Variability in V_r would contradict the iso-potentiality assumed in astrocytic networks (Ma et al., 2016). Reduced coupling has been reported for reactive as well as for proliferating astrocytes (Bordey, Lyons, Hablitz, & Sontheimer, 2001; Gangoso et al., 2012; Tabernero, Jimenez, Velasco, Giaume, & Medina, 2001; Tabernero, Medina, & Giaume, 2006) and may well further contribute to the heterogeneity found in our study.

We found that $K_v4.3$ was expressed in processes of cortical astrocytes as well as astrocytic somata with no differences between non-juxtavascular and juxtavascular astrocytes. Following TBI, reactive astrocytes retained heterogeneous $K_v4.3$ expressions, but the channel proteins were up-regulated in polarized processes of reactive astrocytes. Astrocyte proliferation is often preceded by polarization of astrocytic processes toward the lesion site (Bardehle et al., 2013), and, hence, we suggest that this $K_v4.3$ up-regulation on astrocytic processes could be relevant for subsequent proliferation of a subset of these polarized astrocytes. $K_v4.3$ is one major channel subunit giving rise to A-type currents (I_A), which have been described in astrocytes (Bekar et al., 2005), but were not found in our study; probably because I_A amplitudes are small in astrocytes and therefore masked by larger currents (e.g., $K_{ir}4.1$).

One of our key questions was, if the preponderance of juxtavascular astrocytes to proliferate after injury may be anticipated already by specific hallmarks of these cells prior to injury. Indeed, in this work, we revealed that the expression of $K_v4.3$ in astrocytes was highly determined by their clonal origin in physiological conditions using the *StarTrack* (Garcia-Marques & Lopez-Mascaraque, 2013; Gutierrez et al., 2019), since juxtavascular astrocytes differ in their channel composition from non-juxtavascular astrocytes. Further, not a single sibling cell of pial clones was $K_v4.3$-positive and $K_v4.3$-negative clones were enriched in superficial layers, where astrocyte proliferation is increased. The data, thus, point to a difference of these cells in their ion channel composition and at a potential partial predisposition to proliferate upon certain stimuli, such as TBI. However, the difference between juxtavascular and non-juxtavascular astrocytes was clearly increased after injury, suggesting that injury environment can enlarge astrocyte heterogeneity. The differential properties of juxtavascular astrocytes are important, not only because this may affect the function of neighboring neurons, but also with regard to monocyte invasion. Most monocyte invasion occurs at subpial and vascular contact sides, where proliferation of astrocytes restrains this invasion (Burda, Bernstein, & Sofroniew, 2016; Frik et al., 2018). Given the general beneficial role of astrocyte proliferation in several injury and inflammatory conditions (Anderson et al., 2016; O'Shea, Burda, & Sofroniew, 2017), manipulating ion channels in astrocytes to promote astrocyte proliferation could be a general beneficial to ameliorate the patients' outcome and rehabilitation after different detrimental occurrences like stroke, brain contusions and lesions. Hence, astrocytic K^+ channels might be a target in improving the outcome of stroke, contusion and TBI.

CONFLICT OF INTEREST

The authors declare no potential conflict of interest.

AUTHOR CONTRIBUTIONS

Magdalena Götz originally came up with the idea of this project; Benedikt Grothe, Lars Kunz, and Magdalena Götz further developed and designed the project; Benedikt Grothe and Lars Kunz supervised the main part of the project performed by Stefanie Götz. Laura López-Mascaraque designed the clonal analysis part of the project and supervised Ana Bribian. Stefanie Götz and Ana Bribian (clonal analysis with the StarTrack method) performed the experiments, which were analyzed by Stefanie Götz, Ana Bribian, and Lars Kunz. Lars Kunz and Stefanie Götz wrote the first draft of the manuscript that was revised by Magdalena Götz and Benedikt Grothe. All other authors contributed to the writing of the manuscript.

DATA AVAILABILITY STATEMENT

The data that support the findings of this study are available from the corresponding author upon reasonable request.

ORCID

Laura López-Mascaraque ⬥ https://orcid.org/0000-0002-7154-5687
Magdalena Götz ⬥ https://orcid.org/0000-0003-1551-9203
Lars Kunz ⬥ https://orcid.org/0000-0003-3141-0005

REFERENCES

Adermark, L., & Lovinger, D. M. (2008). Electrophysiological properties and gap junction coupling of striatal astrocytes. *Neurochemistry International*, *52*(7), 1365–1372. https://doi.org/10.1016/j.neuint.2008.02.006

Anderson, M. A., Burda, J. E., Ren, Y., Ao, Y., O'Shea, T. M., Kawaguchi, R., … Sofroniew, M. V. (2016). Astrocyte scar formation aids central nervous system axon regeneration. *Nature*, *532*(7598), 195–200. https://doi.org/10.1038/nature17623

Bardehle, S., Kruger, M., Buggenthin, F., Schwausch, J., Ninkovic, J., Clevers, H., … Gotz, M. (2013). Live imaging of astrocyte responses to acute injury reveals selective juxtavascular proliferation. *Nature Neuroscience*, *16*(5), 580–586. https://doi.org/10.1038/nn.3371

Batiuk, M. Y., Martirosyan, A., Wahis, J., de Vin, F., Marneffe, C., Kusserow, C., … Holt, M. G. (2020). Identification of region-specific astrocyte subtypes at single cell resolution. *Nature Communications*, *11*(1), 1220. https://doi.org/10.1038/s41467-019-14198-8

Bayraktar, O. A., Bartels, T., Holmqvist, S., Kleshchevnikov, V., Martirosyan, A., Polioudakis, D., … Rowitch, D. H. (2020). Astrocyte layers in the mammalian cerebral cortex revealed by a single-cell in situ transcriptomic map. *Nature Neuroscience*, *23*(4), 500–509. https://doi.org/10.1038/s41593-020-0602-1

Bekar, L. K., Loewen, M. E., Cao, K., Sun, X., Leis, J., Wang, R., … Walz, W. (2005). Complex expression and localization of inactivating Kv channels in cultured hippocampal astrocytes. *Journal of Neurophysiology*, *93*(3), 1699–1709. https://doi.org/10.1152/jn.00850.2004

Blackiston, D. J., McLaughlin, K. A., & Levin, M. (2009). Bioelectric controls of cell proliferation: Ion channels, membrane voltage and the cell cycle. *Cell Cycle*, *8*(21), 3527–3536. https://doi.org/10.4161/cc.8.21.9888

Bordey, A., Lyons, S. A., Hablitz, J. J., & Sontheimer, H. (2001). Electrophysiological characteristics of reactive astrocytes in experimental cortical dysplasia. *Journal of Neurophysiology*, *85*(4), 1719–1731. https://doi.org/10.1152/jn.2001.85.4.1719

Bordey, A., & Sontheimer, H. (1997). Postnatal development of ionic currents in rat hippocampal astrocytes in situ. *Journal of Neurophysiology*, *78*(1), 461–477. https://doi.org/10.1152/jn.1997.78.1.461

Bribian, A., Figueres-Onate, M., Martin-Lopez, E., & Lopez-Mascaraque, L. (2016). Decoding astrocyte heterogeneity: New tools for clonal analysis. *Neuroscience*, *323*, 10–19. https://doi.org/10.1016/j.neuroscience.2015.04.036

Burda, J. E., Bernstein, A. M., & Sofroniew, M. V. (2016). Astrocyte roles in traumatic brain injury. *Experimental Neurology*, *275*(Pt 3), 305–315. https://doi.org/10.1016/j.expneurol.2015.03.020

Bush, T. G., Puvanachandra, N., Horner, C. H., Polito, A., Ostenfeld, T., Svendsen, C. N., … Sofroniew, M. V. (1999). Leukocyte infiltration, neuronal degeneration, and neurite outgrowth after ablation of scar-forming, reactive astrocytes in adult transgenic mice. Neuron, 23(2), 297–308. https://doi.org/10.1016/s0896-6273(00)80781-3

Cheng, X., Wang, J., Sun, X., Shao, L., Guo, Z., & Li, Y. (2019). Morphological and functional alterations of astrocytes responding to traumatic brain injury. Journal of Integrative Neuroscience, 18(2), 203–215. https://doi.org/10.31083/j.jin.2019.02.110

Chvatal, A., Pastor, A., Mauch, M., Sykova, E., & Kettenmann, H. (1995). Distinct populations of identified glial cells in the developing rat spinal cord slice: Ion channel properties and cell morphology. The European Journal of Neuroscience, 7(1), 129–142. https://doi.org/10.1111/j.1460-9568.1995.tb01027.x

Cragnolini, A. B., Montenegro, G., Friedman, W. J., & Masco, D. H. (2018). Brain-region specific responses of astrocytes to an in vitro injury and neurotrophins. Molecular and Cellular Neurosciences, 88, 240–248. https://doi.org/10.1016/j.mcn.2018.02.007

Dallerac, G., Chever, O., & Rouach, N. (2013). How do astrocytes shape synaptic transmission? Insights from electrophysiology. Frontiers in Cellular Neuroscience, 7, 159. https://doi.org/10.3389/fncel.2013.00159

Djukic, B., Casper, K. B., Philpot, B. D., Chin, L. S., & McCarthy, K. D. (2007). Conditional knock-out of Kir4.1 leads to glial membrane depolarization, inhibition of potassium and glutamate uptake, and enhanced short-term synaptic potentiation. The Journal of Neuroscience, 27(42), 11354–11365. https://doi.org/10.1523/JNEUROSCI.0723-07.2007

Du, Y., Ma, B., Kiyoshi, C. M., Alford, C. C., Wang, W., & Zhou, M. (2015). Freshly dissociated mature hippocampal astrocytes exhibit passive membrane conductance and low membrane resistance similarly to syncytial coupled astrocytes. Journal of Neurophysiology, 113(10), 3744–3750. https://doi.org/10.1152/jn.00206.2015

Figueres-Onate, M., Garcia-Marques, J., & Lopez-Mascaraque, L. (2016). UbC-StarTrack, a clonal method to target the entire progeny of individual progenitors. Scientific Reports, 6, 33896. https://doi.org/10.1038/srep33896

Frik, J., Merl-Pham, J., Plesnila, N., Mattugini, N., Kjell, J., Kraska, J., … Gotz, M. (2018). Cross-talk between monocyte invasion and astrocyte proliferation regulates scarring in brain injury. EMBO Reports, 19(5), e45294. https://doi.org/10.15252/embr.201745294

Gangoso, E., Ezan, P., Valle-Casuso, J. C., Herrero-Gonzalez, S., Koulakoff, A., Medina, J. M., … Tabernero, A. (2012). Reduced connexin43 expression correlates with c-Src activation, proliferation, and glucose uptake in reactive astrocytes after an excitotoxic insult. Glia, 60(12), 2040–2049. https://doi.org/10.1002/glia.22418

Garcia-Marques, J., & Lopez-Mascaraque, L. (2013). Clonal identity determines astrocyte cortical heterogeneity. Cerebral Cortex, 23(6), 1463–1472. https://doi.org/10.1093/cercor/bhs134

Gupta, R. K., & Prasad, S. (2013). Early down regulation of the glial Kir4.1 and GLT-1 expression in pericontusional cortex of the old male mice subjected to traumatic brain injury. Biogerontology, 14(5), 531–541. https://doi.org/10.1007/s10522-013-9459-y

Gutierrez, Y., Garcia-Marques, J., Liu, X., Fortes-Marco, L., Sanchez-Gonzalez, R., Giaume, C., & Lopez-Mascaraque, L. (2019). Sibling astrocytes share preferential coupling via gap junctions. Glia, 67(10), 1852–1858. https://doi.org/10.1002/glia.23662

Heintz, N. (2004). Gene expression nervous system atlas (GENSAT). Nature Neuroscience, 7(5), 483. https://doi.org/10.1038/nn0504-483

Higashimori, H., & Sontheimer, H. (2007). Role of Kir4.1 channels in growth control of glia. Glia, 55(16), 1668–1679. https://doi.org/10.1002/glia.20574

Honsa, P., Pivonkova, H., Harantova, L., Butenko, O., Kriska, J., Dzamba, D., … Anderova, M. (2014). Increased expression of hyperpolarization-activated cyclic nucleotide-gated (HCN) channels in reactive astrocytes following ischemia. Glia, 62(12), 2004–2021. https://doi.org/10.1002/glia.22721

Isokawa, M., & McKhann, G. M., 2nd. (2005). Electrophysiological and morphological characterization of dentate astrocytes in the hippocampus. Journal of Neurobiology, 65(2), 125–134. https://doi.org/10.1002/neu.20186

Kafitz, K. W., Meier, S. D., Stephan, J., & Rose, C. R. (2008). Developmental profile and properties of sulforhodamine 101—Labeled glial cells in acute brain slices of rat hippocampus. Journal of Neuroscience Methods, 169(1), 84–92. https://doi.org/10.1016/j.jneumeth.2007.11.022

Kelley, K. W., Ben Haim, L., Schirmer, L., Tyzack, G. E., Tolman, M., Miller, J. G., … Rowitch, D. H. (2018). Kir4.1-dependent astrocyte-fast motor neuron interactions are required for peak strength. Neuron, 98(2), 306–319 e307. https://doi.org/10.1016/j.neuron.2018.03.010

Lanjakornsiripan, D., Pior, B. J., Kawaguchi, D., Furutachi, S., Tahara, T., Katsuyama, Y., … Gotoh, Y. (2018). Layer-specific morphological and molecular differences in neocortical astrocytes and their dependence on neuronal layers. Nature Communications, 9(1), 1623. https://doi.org/10.1038/s41467-018-03940-3

Ma, B., Buckalew, R., Du, Y., Kiyoshi, C. M., Alford, C. C., Wang, W., … Zhou, M. (2016). Gap junction coupling confers isopotentiality on astrocyte syncytium. Glia, 64(2), 214–226. https://doi.org/10.1002/glia.22924

MacFarlane, S. N., & Sontheimer, H. (1997). Electrophysiological changes that accompany reactive gliosis in vitro. The Journal of Neuroscience, 17(19), 7316–7329.

MacFarlane, S. N., & Sontheimer, H. (2000). Changes in ion channel expression accompany cell cycle progression of spinal cord astrocytes. Glia, 30(1), 39–48. https://doi.org/10.1002/(SICI)1098-1136(200003)30:1<39::AID-GLIA5>3.0.CO;2-S

Magaki, S. D., Williams, C. K., & Vinters, H. V. (2018). Glial function (and dysfunction) in the normal & ischemic brain. Neuropharmacology, 134(Pt B, 218–225. https://doi.org/10.1016/j.neuropharm.2017.11.009

McKhann, G. M., 2nd, D'Ambrosio, R., & Janigro, D. (1997). Heterogeneity of astrocyte resting membrane potentials and intercellular coupling revealed by whole-cell and gramicidin-perforated patch recordings from cultured neocortical and hippocampal slice astrocytes. The Journal of Neuroscience, 17(18), 6850–6863.

Meme, W., Vandecasteele, M., Giaume, C., & Venance, L. (2009). Electrical coupling between hippocampal astrocytes in rat brain slices. Neuroscience Research, 63(4), 236–243. https://doi.org/10.1016/j.neures.2008.12.008

Mishima, T., & Hirase, H. (2010). In vivo intracellular recording suggests that gray matter astrocytes in mature cerebral cortex and hippocampus are electrophysiologically homogeneous. The Journal of Neuroscience, 30(8), 3093–3100. https://doi.org/10.1523/JNEUROSCI.5065-09.2010

Mishima, T., Sakatani, S., & Hirase, H. (2007). Intracellular labeling of single cortical astrocytes in vivo. Journal of Neuroscience Methods, 166(1), 32–40. https://doi.org/10.1016/j.jneumeth.2007.06.021

Morel, L., Chiang, M. S. R., Higashimori, H., Shoneye, T., Iyer, L. K., Yelick, J., … Yang, Y. (2017). Molecular and functional properties of regional astrocytes in the adult brain. The Journal of Neuroscience, 37(36), 8706–8717. https://doi.org/10.1523/JNEUROSCI.3956-16.2017

Moroni, R. F., Inverardi, F., Regondi, M. C., Pennacchio, P., & Frassoni, C. (2015). Developmental expression of Kir4.1 in astrocytes and oligodendrocytes of rat somatosensory cortex and hippocampus. International Journal of Developmental Neuroscience, 47(Pt B, 198–205. https://doi.org/10.1016/j.ijdevneu.2015.09.004

Nwaobi, S. E., Cuddapah, V. A., Patterson, K. C., Randolph, A. C., & Olsen, M. L. (2016). The role of glial-specific Kir4.1 in normal and pathological states of the CNS. Acta Neuropathologica, 132(1), 1–21. https://doi.org/10.1007/s00401-016-1553-1

Olsen, M. L., Campbell, S. C., McFerrin, M. B., Floyd, C. L., & Sontheimer, H. (2010). Spinal cord injury causes a wide-spread, persistent loss of Kir4.1 and glutamate transporter 1: Benefit of 17 beta-

oestradiol treatment. *Brain*, *133*(Pt 4), 1013–1025. https://doi.org/10.1093/brain/awq049

Olsen, M. L., & Sontheimer, H. (2004). Mislocalization of Kir channels in malignant glia. *Glia*, *46*(1), 63–73. https://doi.org/10.1002/glia.10346

O'Shea, T. M., Burda, J. E., & Sofroniew, M. V. (2017). Cell biology of spinal cord injury and repair. *The Journal of Clinical Investigation*, *127*(9), 3259–3270. https://doi.org/10.1172/JCI90608

Pivonkova, H., Benesova, J., Butenko, O., Chvatal, A., & Anderova, M. (2010). Impact of global cerebral ischemia on K+ channel expression and membrane properties of glial cells in the rat hippocampus. *Neurochemistry International*, *57*(7), 783–794. https://doi.org/10.1016/j.neuint.2010.08.016

Robel, S., Berninger, B., & Gotz, M. (2011). The stem cell potential of glia: Lessons from reactive gliosis. *Nature Reviews. Neuroscience*, *12*(2), 88–104. https://doi.org/10.1038/nrn2978

Schools, G. P., Zhou, M., & Kimelberg, H. K. (2006). Development of gap junctions in hippocampal astrocytes: Evidence that whole cell electrophysiological phenotype is an intrinsic property of the individual cell. *Journal of Neurophysiology*, *96*(3), 1383–1392. https://doi.org/10.1152/jn.00449.2006

Seifert, G., Henneberger, C., & Steinhauser, C. (2018). Diversity of astrocyte potassium channels: An update. *Brain Research Bulletin*, *136*, 26–36. https://doi.org/10.1016/j.brainresbull.2016.12.002

Seifert, G., Huttmann, K., Binder, D. K., Hartmann, C., Wyczynski, A., Neusch, C., & Steinhauser, C. (2009). Analysis of astroglial K+ channel expression in the developing hippocampus reveals a predominant role of the Kir4.1 subunit. *The Journal of Neuroscience*, *29*(23), 7474–7488. https://doi.org/10.1523/JNEUROSCI.3790-08.2009

Sirko, S., Behrendt, G., Johansson, P. A., Tripathi, P., Costa, M., Bek, S., … Gotz, M. (2013). Reactive glia in the injured brain acquire stem cell properties in response to sonic hedgehog. [corrected]. *Cell Stem Cell*, *12*(4), 426–439. https://doi.org/10.1016/j.stem.2013.01.019

Sontheimer, H. (1994). Voltage-dependent ion channels in glial cells. *Glia*, *11*(2), 156–172. https://doi.org/10.1002/glia.440110210

Stephan, J., & Friauf, E. (2014). Functional analysis of the inhibitory neurotransmitter transporters GlyT1, GAT-1, and GAT-3 in astrocytes of the lateral superior olive. *Glia*, *62*(12), 1992–2003. https://doi.org/10.1002/glia.22720

Tabernero, A., Jimenez, C., Velasco, A., Giaume, C., & Medina, J. M. (2001). The enhancement of glucose uptake caused by the collapse of gap junction communication is due to an increase in astrocyte proliferation. *Journal of Neurochemistry*, *78*(4), 890–898. https://doi.org/10.1046/j.1471-4159.2001.00476.x

Tabernero, A., Medina, J. M., & Giaume, C. (2006). Glucose metabolism and proliferation in glia: Role of astrocytic gap junctions. *Journal of Neurochemistry*, *99*(4), 1049–1061. https://doi.org/10.1111/j.1471-4159.2006.04088.x

Urrego, D., Tomczak, A. P., Zahed, F., Stuhmer, W., & Pardo, L. A. (2014). Potassium channels in cell cycle and cell proliferation. *Philosophical Transactions of the Royal Society of London. Series B, Biological Sciences*, *369*(1638), 20130094. https://doi.org/10.1098/rstb.2013.0094

Verkhratsky, A., & Nedergaard, M. (2018). Physiology of Astroglia. *Physiological Reviews*, *98*(1), 239–389. https://doi.org/10.1152/physrev.00042.2016

Westergard, T., & Rothstein, J. D. (2020). Astrocyte diversity: Current insights and future directions. *Neurochemical Research*, *45*(6), 1298–1305. https://doi.org/10.1007/s11064-020-02959-7

Zhou, M., Schools, G. P., & Kimelberg, H. K. (2006). Development of GLAST(+) astrocytes and NG2(+) glia in rat hippocampus CA1: Mature astrocytes are electrophysiologically passive. *Journal of Neurophysiology*, *95*(1), 134–143. https://doi.org/10.1152/jn.00570.2005

SUPPORTING INFORMATION

Additional supporting information may be found online in the Supporting Information section at the end of this article.